

JUN 06 1988

G H

# Acoustic Backscattering From the Basin and Margins of the Arctic Ocean

I. DYER, A. B. BAGGEROER,<sup>1</sup> J. D. ZITTEL,<sup>2,3</sup> AND R. J. WILLIAMS

Department of Ocean Engineering, Massachusetts Institute of Technology, Cambridge, Massachusetts 02139

Sound waves created by high-energy explosives were used to measure reverberation and backscattering in the Arctic Ocean. From an ice camp in the Beaufort Sea, signals were backscattered from the continental margin and other major features of the basin. An acoustic array was used to analyze the signals in azimuth. Based on these data we constructed charts of normalized backscatter level, which can be compared with known topography of the Arctic Ocean. Resolution of this remote sensing technique for our experimental conditions (analysis frequency, 9 Hz; averaging time, 20 s; array size,  $600 \times 600$  m) is about 8° in azimuth, 15 km in radial extent, and 1 km in depth. We obtained interpretable signals out to 2700 km. For 1000 km or less, the backscatter charts provide continuous coverage of the margins and major submerged features. Strong returns from about 73.2°N, 139.0°W indicate one or more prominent features that many contemporary topographic charts do not show, but which we believe to be real. Other strong returns are evident from the Northwind Escarpment and from the continental slopes of Alaska and the Canadian Archipelago. Via a backscatter model, we estimate the roughness product (rms height times correlation radius) of these features to be about 4500 m<sup>2</sup> on average.

## 1. INTRODUCTION

In March and April 1978, an ice camp was established and occupied in the Arctic Ocean to remotely measure several topographic and geophysical properties of the ocean boundaries. The camp was located approximately at 73.5°N and 150.5°W in the Beaufort Sea over the Canada Abyssal Plain, where the water depth is about 3800 m. We report here on acoustic backscattering from the entire ocean basin and its margins, the major features of which are shown in Figure 1.

The experiment, known as CANBARX (Canada Basin Acoustic Reverberation Experiment), used a two-dimensional horizontal array to receive the backscattered acoustic signals. Sound was created at the camp's location with high-energy explosives and took as long as 3600 s to reach and return from physiographic features 2700 km away. Interest in such backscattered signals is two-fold. First, the ocean can be used as a long-range acoustic communication channel, and the effect of features such as shown in Figure 1 needs to be understood. Second, the backscattered signals carry information on the nature and location of these features, thus affording wide-area knowledge from a single measurement location, including the possibility of identifying unknown features and/or features of unusual relief. As will be seen, the CANBARX array (and our processing method) averages over or ignores certain features, but in demonstrating the attributes of the experimental method we hope to point the way to future higher-resolution experiments, as well as to present some new physical results.

Acoustic backscattering (reverberation) on a basin-wide scale has been previously measured. Mellen and Marsh [1963] noted that 'reverberation in the Arctic is observable for no less than 30 minutes after an explosive detonation of

moderate size.' Kutschale [1969] observed the effects of bottom topography, also in the Arctic, on both propagation and reverberation. Reverberation in the North Atlantic Basin was measured and modeled by Goertner and Blatstein [1975] and Blatstein [1978], again with the use of explosive sources. The essential distinction between the previous and present work is our use of an array to analyze signals received as a function of horizontal angle. Such spatial analyses support identification of specific features in both azimuth and range and provide detail heretofore unavailable.

In the course of CANBARX, other important Arctic properties were measured, including ambient noise and, via refraction and reflection experiments, bottom phase speeds and layer thicknesses. Papers are in preparation and in press on these results [Baggeroer and Falconer, 1982].

## 2. DATA ACQUISITION AND PROCESSING

The camp was established on new ice approximately 2 m thick, with pressure ridges and old ice, and hence much greater thicknesses, about 1-3 km away, depending upon direction. Holes were drilled in the 2 m ice for the array, which was arranged as shown in Figure 2. All 11 hydrophones of the array were suspended to a depth of 61 m and were spaced logarithmically in the horizontal along two orthogonal legs. The array's aperture is somewhat over five wavelengths for data at 9 Hz to be presented here.

Recordings were made for up to 4800 s after the shot instant on a 12 channel digital acquisition system; a typical channel is schematically illustrated in Figure 3. An important feature is the gain ranging amplifier which provided a dynamic range of 120 dB, enabling acquisition of very low level signals backscattered from remote areas, as well as higher levels from closer regions. Through its rapid response, it also enabled acquisition of lower levels in the vicinity of a strong scatterer, along with the high level from the scatterer.

Some processing was done at the camp to assure adequate data quality and to help guide the experimental program. The bulk of the data, however, was processed thereafter. Processing steps are shown schematically in Figure 4. For results presented here, the data were analyzed in 3 Hz bands

<sup>1</sup> Also at Department of Electrical Engineering and Computer Science, Massachusetts Institute of Technology, Cambridge, Massachusetts 02139.

<sup>2</sup> Also at Department of Ocean Engineering, Woods Hole Oceanographic Institution, Woods Hole, Massachusetts 02543.

<sup>3</sup> Now at Applied Physics Laboratory, The Johns Hopkins University, Laurel, Maryland 20810.

JTC FILE COPY

AD-A196 338

DISTRIBUTION STATEMENT A

Approved for public release;

Distribution Unlimited

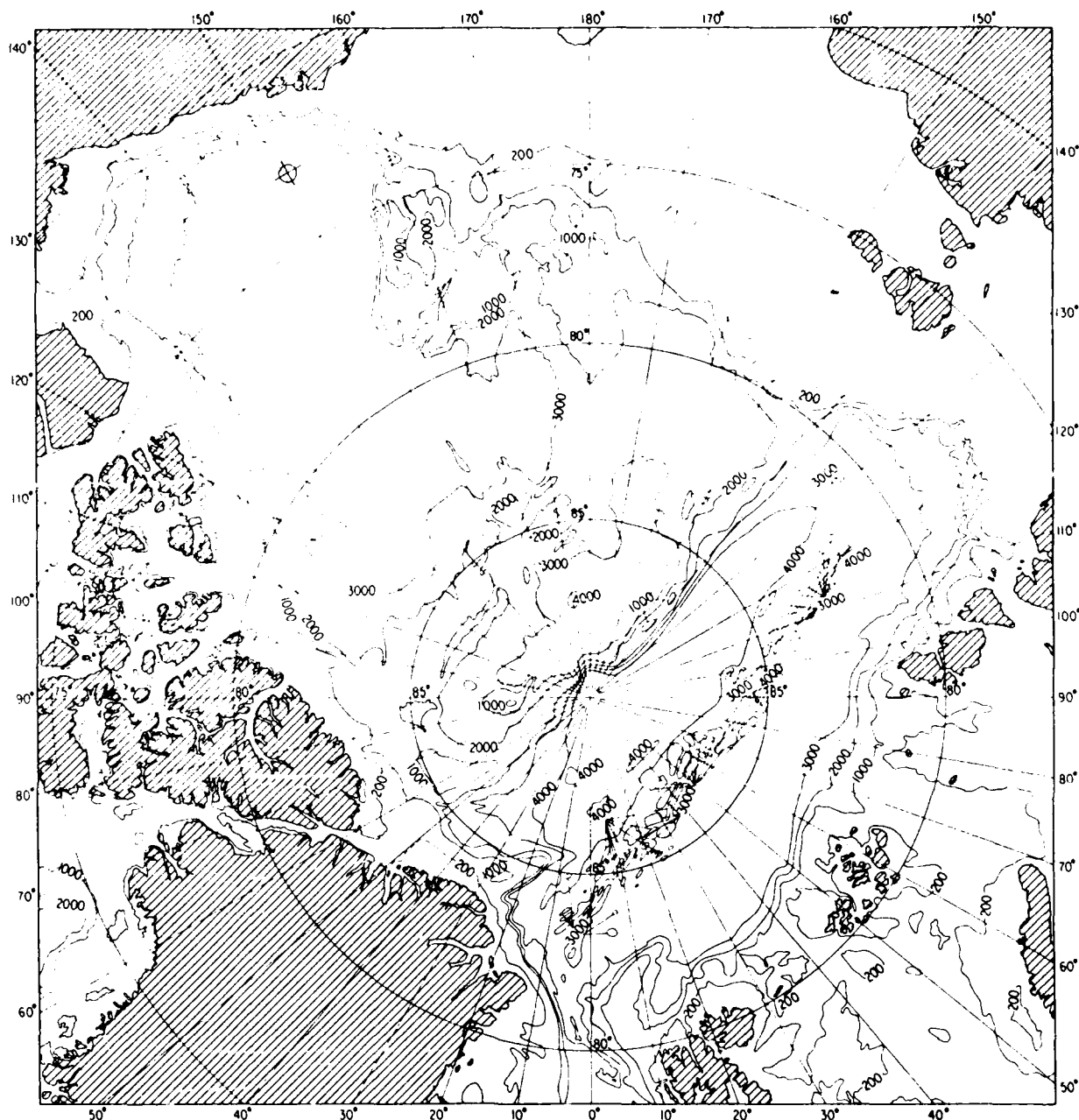


Fig. 1. Major features of the Arctic Ocean basin. Some of them, with approximate coordinates, are Barrow (Alaskan) coast (75°N, 140°-160°W), Canadian archipelago (78°-83°N, 60°-125°W), Greenland coast (83°N, 10°-60°W), European and Asian margin (80°N, 10°-160°E), Chuckchi Cap (78°N, 160°-180°W), Northwind Escarpment (75°-79°N, 155°W), Alpha ridge (85°N, 90°-180°W), Lomonosov ridge (along about 80°N, 140°E through the North Pole to about 85°N, 60°W). Redrawn from *Canadian Hydrographic Service* [1979]. The encircled cross is the source/array location of CANBARX.

centered on 9 Hz, and beamforming was accomplished via the maximum likelihood method [Baggeroer, 1978; Capon, 1979; McDonough, 1979] to yield an azimuthal resolution of about 8° (0.14 rad) for the signal/noise ratios typically encountered.

The beamformed sound signals are highly time dependent, due not only to the impulsive sound source but also to highly variable backscattering in time (range). With a signal sampling rate of 250 Hz, we formed estimates of the time-dependent pressure spectral density by averaging the signal over both the 3 Hz bandwidth and a 20 s time window. The

time window was moved forward in 4 s steps and gave a set of data points versus time for each bearing. Finally, the bearing was swept through 360° in 6° steps, to yield an array of data points pertinent to basin backscattering. Reasons for and implications of the choice of the 20 s time window and the 9 Hz center frequency will be explicitly discussed in this paper.

To generate impulsive sources of sound, we exploded TNT at a pressure depth of 244 m, with a range in mass from 50 to 400 kg, mostly at 200 kg. A source level monitor occupied the 12th channel of the data acquisition system,

A-1 21

using a hydrophone of much lower sensitivity than the other 11 in the array. But the monitor hydrophone was deployed improperly just below the ice making interpretation next to impossible. It was too close to a pressure release surface and a region of layered cavitation induced by the intense reflected signal [Malme *et al.*, 1964; Gaspin *et al.*, 1979]. Instead of measured source data, we rely therefore upon standard values for underwater TNT explosions, the most comprehensive results coming from the formulas and charts of Weston [1960] and Urick [1975]. Values taken from these publications, and detailed intercomparisons of CANBARX backscatter data, indicate that the maximum uncertainty in source level, with the use of this procedure, is  $\pm 3$  dB, including all other uncertainties in signal level (due to calibration, voltage standards, etc.). The relative uncertainty in our data, however, is less than 1 dB.

In many ways the Beaufort Sea ice cover in March and April is an excellent platform for scientific work. It, however, is known to drift under action of wind and/or current stress. During our experiment the camp remained within an ellipse of about 4 km N-S semi-axis, and 7 km E-W semi-axis. It also rotated with a standard deviation of about  $2^\circ$ . Both motions appear random. We have not corrected our backscatter data for these motions, since they fall well within other uncertainties in or averages over the data, and in any case have small effect in relation to the wide-area perspective of our experiment.

### 3. REVERBERATION DATA

We form the reverberation level

$$RL_{T_p} = 10 \log \frac{T_p \langle S(f_0, t) \rangle}{A(f_0)} \quad \text{dB re 1 m} \quad (1)$$

where  $4\pi A(f_0)/\rho c$  is equal to source energy ( $\rho$  water density and  $c$  sound speed);  $S(f_0, t)$  is the spectral density of  $p^2(t)$ , the sound pressure squared;  $T_p$  is the processor averaging time; and where  $\langle \dots \rangle$  indicates the average over both  $T_p$  and bandwidth  $W_p$ .

In our study we chose values of  $f_0 = 9$  Hz,  $W_p = 3$  Hz.

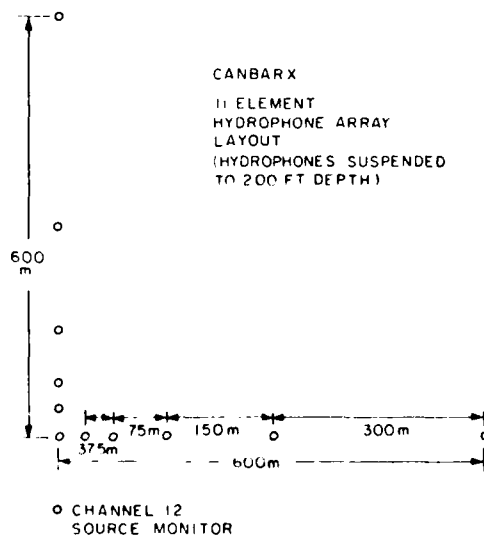


Fig. 2. Layout of the hydrophone array. The array is 200 ft (61 m) below the upper surface of the ice.

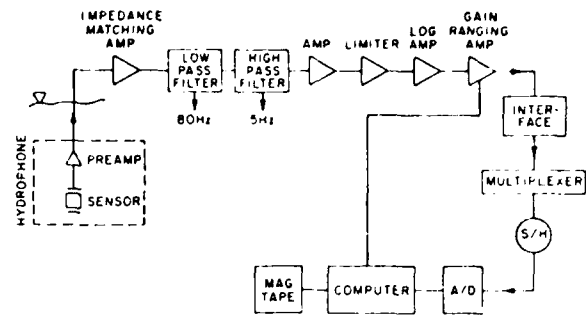


Fig. 3. Recording system for each channel

and  $T_p = 20$  s. To the extent that  $S(f_0, t)$  is uniformly distributed over at least 20 s,

$$RL_{T_p, 20} = RL_{20} + 10 \log \frac{T_p}{20} \quad (2)$$

and subsequently we shall argue that this is so, at least approximately, for the signals of interest.

The integrated source spectral density at the frequency  $f_0$  is

$$A(f_0) = \int_0^{T_s} S_s(f_0, t) dt \quad (3)$$

where  $T_s$  is the duration of the explosion and  $S_s$  is the spectral density evaluated at the reference distance of 1 m from the source. The explosion duration  $T_s$  is about 0.3 s, but as indicated earlier we use standard values of  $A(f_0)$  rather than perform the integration in (3) with measured values of  $S_s(f_0, t)$ .

A three-dimensional view of  $RL_{20}$  versus bearing and time, Figure 5, shows significant structure in the backscattered sound field out to the maximum displayed, 3600 s (3431 s after shot instant). The level at the shot time (169 s) is not physical, representing saturation of the sensitive hydrophone-preamplifier sensors of the array. Thereafter, the sensors recover and display  $RL_{20}$ , initially with significant structure through  $360^\circ$ , and then increasingly with confinement toward the northerly sector as the signals return from more northerly regions of the basin. (Curiously, Figure 5 shows noise, at say  $180^\circ$  true and 3600 s, to be less than that before the shot, an effect often observed and to be described more fully in another paper on ambient noise. In brief, for low ice stress and therefore low noise conditions, an explosion relieves stress and reduces the noise nearby for some hours thereafter.)

Contour diagrams of  $RL_{20}$  are more suitable for quantitative interpretation. An example is shown in Figure 6. With the aid of the overlay of the basin's major features, one can discern significant returns from the Barrow Coast to the south, from the Canadian Archipelago to the southeast and east, and from the Northwind Escarpment to the west. An extensive set of reverberation diagrams, from which the one shown here is taken, is available [Zittel, 1979].

With appeal to linearity, a reverberation diagram such as Figure 6 can be applied directly to a wide class of acoustic communication problems [Urlick, 1975]. It will become obvious in the next section, however, that such results are in general specific to  $f_0$ , to the source/receiver depths, and to their geographic location.

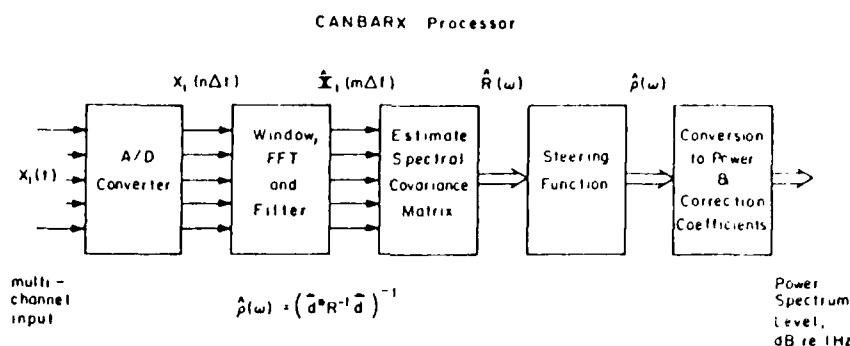


Fig. 4. Block diagram of the array processor.

#### 4. CONVERSION OF REVERBERATION TO BACKSCATTER DATA

Further processing of reverberation diagrams is needed when the objective is better understanding of physiographic features. As may be seen in Figure 6, for example, contours enclosing scatterers at a given  $RL_{20}$  may extend over a considerable range. Surely, a scatterer at large range is far more important than one at small range with the same  $RL_{20}$ . Also, reverberation diagrams give no guidance on the depth of important scatterers. We will show that the CANBARX source/receiver combination emphasizes scatterers in the upper part of the water column. We will also normalize the reverberation data to reduce range-dependent effects, thereby facilitating identification of physiographic features and quantitative comparison among them.

##### 4.1 One-Way Propagation in an Ideal Channel

The sound speed profile in the Arctic Ocean is approximately a linear function of increasing depth, with some deviations in the upper 500 m or so which we shall ignore. Thus, all acoustic rays follow upward refracting paths that

are to a good approximation circular arcs. From Snell's Law, the water depth  $D_1$  and source depth  $z_1$  determine the maximum ray angle  $\theta_1$ , (in small angle approximation):

$$\theta_1^2 \approx \frac{2g(D_1 - z_1)}{c_1} \quad (4)$$

where  $g$  is the sound speed gradient, and  $c_1$  the sound speed at the source depth. In this model, all rays described by  $|\theta| < \theta_1$  follow refracted paths completely in the water column, reflecting periodically from the ice canopy, while rays  $|\theta| > \theta_1$  travel at least partially in the bottom. As is customary, we neglect the latter because bottom paths are known to have much higher attenuations than water paths. With  $g = 1.85 \times 10^{-2} \text{ s}^{-1}$ ,  $c_1 = 1.45 \text{ km/s}$ , and  $D_1 - z_1 = 3560 \text{ m}$  as typical values, we have  $\theta_1 = 0.30$ , which is small enough for use of small angle approximations whenever convenient. Also, at 9 Hz the array steered in the horizontal emphasizes returns from within  $|\theta| \leq 0.4$ , further justifying the neglect of bottom interacting paths.

We neglect cavitation which is expected at the water-ice interface in the vicinity of the source, and defer its discus-

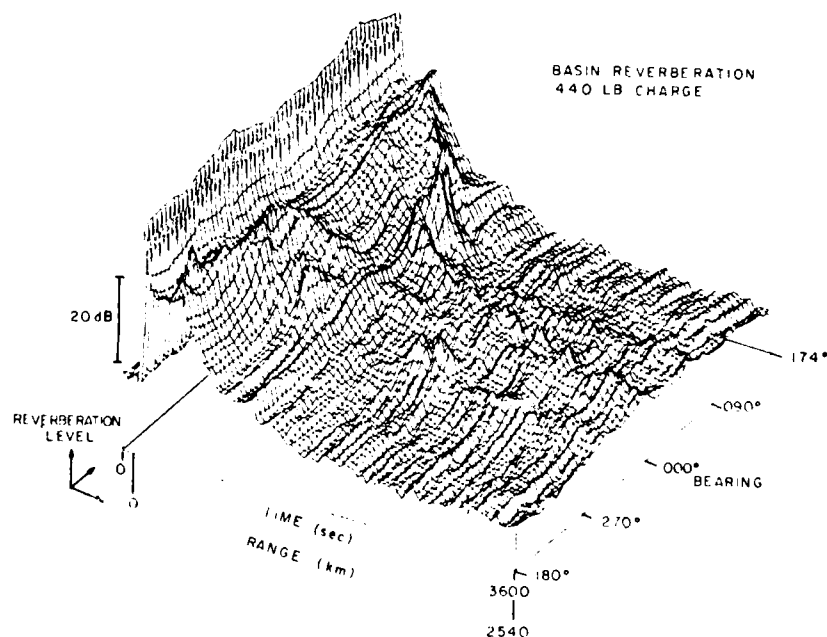


Fig. 5. Reverberation level,  $RL_{20}$ , on a relative basis versus bearing (geographic true) and time. Charge weight 200 kg, source depth 244 m, receiver depth 61 m, center frequency 9 Hz. A nominal sound speed of 1.48 km/s is used to fix a range scale (experiment 13).

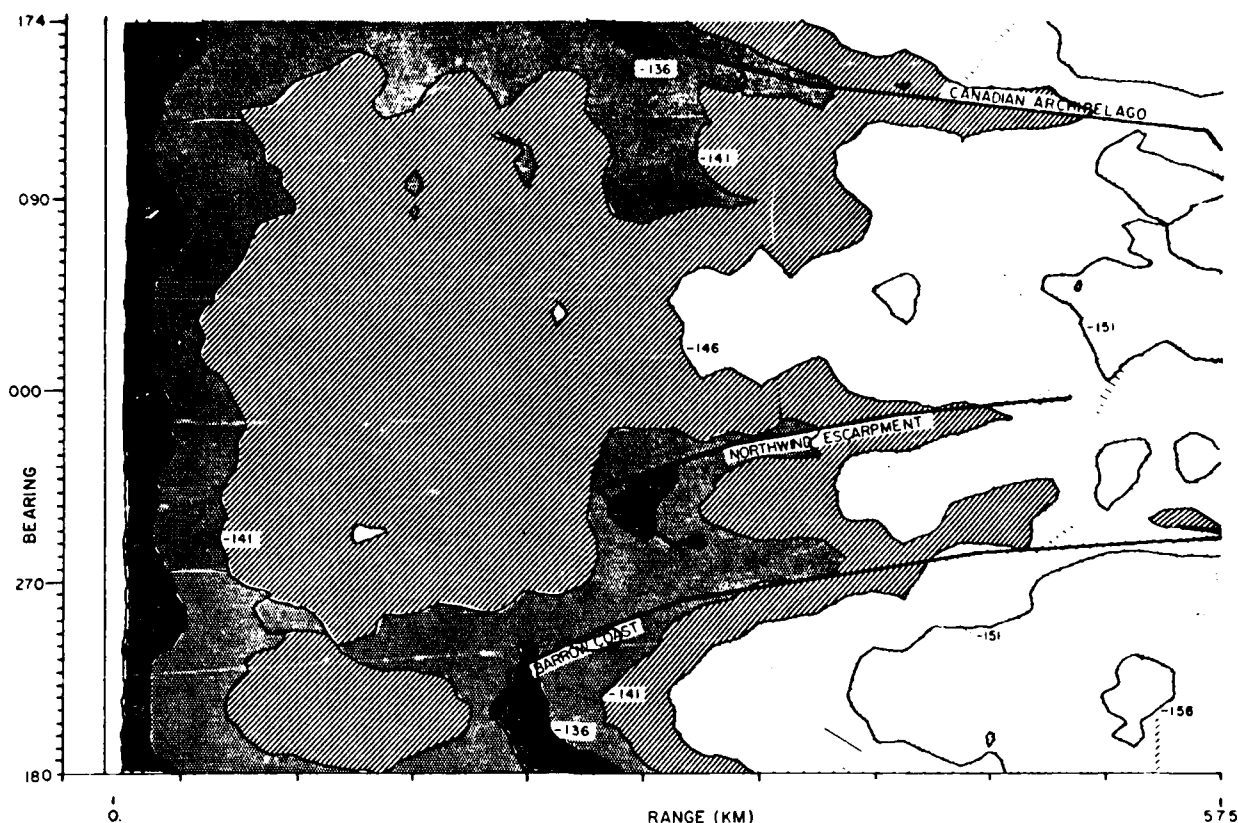


Fig. 6. Contours of  $RL_{20}$  in dB re 1 m. Charge weight 50 kg [ $A(9 \text{ Hz}) = 2 \times 10^{22} \mu\text{Pa}^2 \text{ m}^{-2} \text{ s Hz}^{-1}$ ] (experiment 31). Noncontour lines are 200 m depths from known topography. The Northwind Escarpment (at  $\sim 800 \text{ m}$ ) is also shown.

sion for the end of this section. Following Smith [1971, 1974] we assume the source to be a delta function and write

$$S(f, t) = \frac{4A(f)e^{-aR}}{R} \int_{\theta_m}^{\theta_1} \frac{\delta t - (T_1 - (R\theta^2/6c_1))d\theta}{X(\theta) \tan |\phi|} \quad (5)$$

which is a ray averaged expression for the sound field. In this equation  $X(\theta)$  is the ray period (cycle distance),  $R$  is the horizontal range,  $a$  is the attenuation coefficient (based on loss which is assumed a linear function of ray angle),  $\phi$  is the ray angle of the  $\theta$  ray as it travels through the water column and is given by

$$\phi^2 \approx \theta^2 - \frac{2g(z - z_1)}{c_1} \quad (6)$$

where  $z$  is the depth measured in the positive sense from the ocean top to the bottom  $D_1$ . Since  $\phi$  can not be complex, we see from (6) that the integral's lower limit is  $\theta_m = 0$  for observation above ( $z < z_1$ ) and  $\theta_m = [2g(z - z_1)/c_1]^{1/2}$  for observation below ( $z > z_1$ ) the source.

We note that (5) describes a pulse first arriving at a time after shot instant given by  $T_1 - R\theta_1^2/6c_1$  and culminating at  $T_1 - R\theta_m^2/6c_1$ . Its duration  $\Delta t$  is, therefore,

$$\frac{6c_1\Delta t}{R\theta_1^2} = \begin{cases} 1 & z < z_1 \\ 1 - \frac{z - z_1}{D_1 - z_1} & z > z_1 \end{cases} \quad (7)$$

[ $T_1$  is given by  $(R/c_1)(1 - (2gz_1/3c_1))$ ]. For values of  $R$  and  $z$  of interest in the CANBARX data,  $\Delta t$  greatly exceeds the explosion duration  $T_s$ , thus justifying the delta function

assumption. The (integrable) singularities in (5) [Weston, 1980] predict that most of the pulse energy is concentrated at its culmination, as experiments in the Arctic verify [DiNapoli et al., 1978]. While it might be tempting to use actual source shapes  $S_s(f, t)$  in convolution with (5) to better predict the shape of  $S(f, t)$  at its peak, we need not do so, since ultimately we shall average  $S(f, t)$  in a way that suppresses this detail.

As indicated in the foregoing, cavitation at the top of the water column adversely affected our measurement of source strength. The hydrophone deployed for this measurement at times was in the cavity region, and the pressures recorded were therefore unreliable indicators of source properties. On the other hand, in (5), which describes the sound field, we neglected cavitation and we now justify this. For shots used in our experiment (50 to 400 kg TNT detonated at 244 m) the spectral peaks are in the 3 Hz band centered at 9 Hz. These peaks are dominated by the bubble energy and, unlike the shock wave energy, reflect from the top of the water column as do infinitesimal signals [Gaspin et al., 1979]. Thus (5) may be properly applied to our experiment.

#### 4.2 Effective Channel Depth

The time integral of (5) gives the energy profile in  $z$ , a few values of which are given in Table 1. We see a substantial bias toward energy in the upper part of the water column. Also, on average, the energy levels above 500 m are about equal to that found at 500 m. (The energy profile predicted by (5) is singular at 244 m, the source depth, a well-known failing of ray theory. Wave theory would give the proper finite result but it would not sensibly affect the definition of

TABLE 1. Acoustic Energy Depth Profile (Approximate)

Depth, m	Energy Level, dB re Level at 500 m	Gradient of Energy Level
500	0	-1 dB/100 m
800	-2	-1 dB/200 m
1200	-4	-1 dB/300 m
1900	-6	-1 dB/400 m

Source at 244 m.

effective channel depth.) Thus, we can define an effective depth  $D_e$  such that the region  $0 \leq z \leq D_e$  contains the acoustic energy important to backscattering. The half-energy depth is at about 1000 m, and setting  $D_e = 1000$  m is a natural, although crude, definition of the effective channel depth. We note that others have made similar definitions [e.g., Buck, 1981].

A scattering feature below 2000 m, for example, would be expected to be irradiated by at least 6 dB less energy than one at 500 m or above, and hence such deep features are not likely to be important in backscattering diagrams. Thus we should expect the continental margin, rather than mid-ocean features, to be the principal locus of backscattering.

We may associate with  $D_e$  an effective source ray  $\theta_e$  such that  $|\theta| \leq \theta_e$  describes the region of energy important to backscattering. For  $D_e = 1000$  m we have  $\theta_e = 0.14$ , and this source angle replaces  $\theta_1$  in the integral of (5) for the incident acoustic field.

#### 4.3 Wedge Model of Physiographic Features

Signals described by (5) are scattered by any physical feature departing from the ideal constant-gradient constant-depth channel. We consider only departures from the latter and restrict attention to features measurable in the scale of basin dimensions, such as the continental margin.

We hypothesize that a major feature may be modeled as a wedge of angle  $\beta$ , with the incident plane of sound at the angle  $\gamma$  to the wedge (see Figure 7). The ray angle  $\phi$  at the wedge then has a grazing angle to the wedge of  $\phi + \psi$ , where  $\psi$  is the in-plane wedge angle determined by

$$\Psi \equiv \tan \psi = \tan \beta \cos \gamma \quad (8)$$

The plane defined by  $\beta$  is in actuality the mean of a rough surface, and we concentrate here on suitable characterization of this plane for basin backscattering. The angles  $\beta$  and  $\gamma$  can be estimated at each location from present knowledge of the basin and its features. But we prefer to consider them as stochastic variables with estimated or assumed statistics and density functions. Ultimately, data from diversely located backscatter experiments might be useful in determining  $\beta$  and  $\gamma$  independently, but for present purposes we adopt the stochastic view as the more direct way of gaining an appreciation of basin backscattering.

We assume  $B \equiv \tan \beta$  has a Rayleigh probability density function (pdf), with mean  $\mu_B$  and variance  $\sigma_B^2 = \mu_B^2 ((4/\pi) - 1)$ . The assumed pdf as such is not crucial, but when sampling over a large number of wedges, we take it as likely that the pdf is skewed towards the smaller values of  $B$ . We also assume that the pdf for  $\gamma$  is uniform in the interval  $(-\pi/2, \pi/2)$  and hence that  $G \equiv \cos \gamma$  has a pdf with  $\mu_G = 2/\pi$  and  $\sigma_G^2 = 1/2 - 4/\pi^2$ . Again the precise form of the assumed pdf is not crucial, and is applicable principally as an ensemble description of the basin's physiographic features. With these

pdfs it readily can be shown that the pdf for  $\Psi$  is half-Gaussian, with  $\mu_\Psi = 2\mu_B/\pi$  and  $\sigma_\Psi^2 = \mu_B^2(1 - 2/\pi)/\pi$ . Such a statistical view of Arctic Ocean features is offered not as a proven experimental fact, but rather as a plausible model whose use can help in interpreting backscatter data.

In a similar vein, the wedge angle  $\psi'$  in the plane of a wave front is given by

$$\Psi' \equiv \tan \psi' = \tan \beta |\sin \gamma| \quad (9)$$

and has a pdf and statistics identical to those of  $\Psi$ .

Locally, a wedge restricts the ray angle  $\phi$  to

$$0 \leq \phi + \psi \leq (4\psi\theta)^{1/2} \quad (10)$$

The lower limit clearly restricts rays from incidence beneath the wedge, while the upper limit can be shown to restrict scattering from the wedge to first-order scattering only. These restrictions, together with (6), describe the variation of  $\phi$  with depth  $z$  on the wedge.

One immediately can see that backscattering from Arctic Ocean physiographic features is governed by quite small ray angles. If we take  $\mu_\Psi = 3 \times 10^{-2}$  ( $\mu_\Psi \approx 1.7^\circ$ ,  $\mu_B \approx 2.7^\circ$ ) and note from (10) that the maximum values of  $(\phi + \psi)^2$  are distributed as  $\psi|\theta|$ , then  $(\phi + \psi)_{\text{rms}}$  is less than  $1.3 \times 10^{-1}$ , i.e.,  $7.6^\circ$ , for  $\theta$  less than  $\theta_e$ .

In addition to  $\beta$  and  $\gamma$ , the transverse width of a wedge,  $l$ , affects the backscattering of sound. We hypothesize that this is approximated by its longitudinal width,

$$l = z_w \cot \beta \quad (11)$$

where  $z_w$  is the wedge's height (see Figure 7). Our view of a physiographic feature is thus of a string of wedges, each wedge characterized by its slope  $\tan \beta$  and its orientation  $\gamma$  referred to the sound wave vector. The slope and orientation have a horizontally isotropic scale  $l$ , which itself can be considered a stochastic variable via  $\beta$  and  $z_w$ . We shall not, however, attempt to specify its stochastic variation explicitly.

#### 4.4 Overlap of the Sound Field With Physiographic Features

Irradiated wedges representing a section of the continental margin are potentially capable of scattering energy back toward the receiving array. In our processing system, backscattering ultimately is observed through a bearing window  $\xi_p$  (0.14 rad) and a time window  $T_p$  (20 s). The overlap of the acoustic area defined by these windows with the horizontal

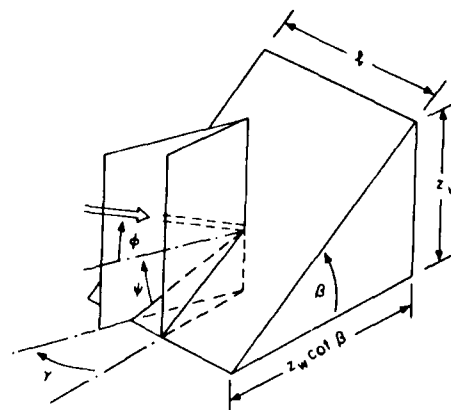


Fig. 7. Wedge model.

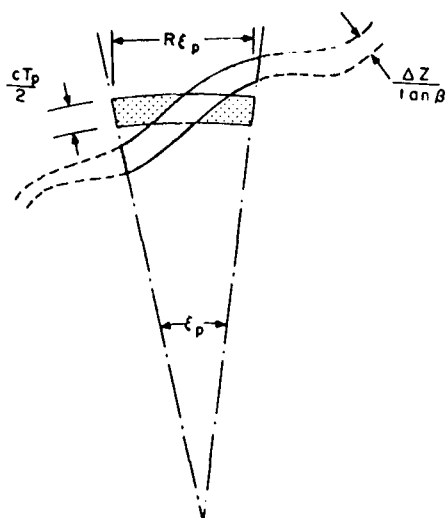


Fig. 8. Acoustic sector overlaying the horizontal projection of a physiographic feature.

projection of a feature is shown in Figure 8. From this, we can find the ratio  $\Gamma$  of included or irradiated wedge area to acoustic window area, and its various values are given in Table 2. The quantity  $\Delta z$  is the vertical extent of the feature, an estimate of which follows from the vertical coverage of the sound field and from dimensions of the feature itself. (See Figure 9.) In particular, the acoustic field has a lower channel depth  $D_e \approx 1000$  m, so that the continental slope normally would not be sensed down to its transition to the continental rise. Also the slope extends up to  $D_s$ , its transition to the shelf. Hence,  $\Delta z = D_e - D_s$ , and with a nominal value  $D_s = 200$  m, we estimate  $\Delta z \approx 800$  m.

In composing Table 2 we have assumed the scale  $l$  of (11) to be larger than the scale of the irradiated wedge, which permits us to think of a single value of  $\Psi$  or  $\Psi'$  for each overlap. This assumption is not restrictive, because ultimately we shall treat  $\Gamma$  both approximately and as a stochastic variable, the latter implicitly allowing  $\Psi$  (and  $\Psi'$ ) to change within the scale of an irradiated wedge. Incidence angles  $\gamma_0$  and  $\gamma_1$  in Table 2 are given by

$$\begin{aligned} \tan \gamma_0 &= \frac{2\Delta z}{cT_p\Psi} \\ \tan \gamma_1 &= \frac{cT_p}{2R\xi_p} \end{aligned} \quad (12)$$

TABLE 2. Values of  $\Gamma$ , the Ratio of Irradiated Wedge Area to Acoustic Window Area

$\Psi < \frac{2\Delta z}{cT_p}$		$\Psi > \frac{2\Delta z}{cT_p}$	
		1, $\gamma < \gamma_0$	
$R\Psi' < \frac{\Delta z}{\xi_p}$	1	$\frac{2\Delta z}{cT_p\Psi'}$ , $\gamma > \gamma_0$	
		$\frac{2\Delta z}{cT_p\Psi}$ , $\gamma < \gamma_1$	
$R\Psi' > \frac{\Delta z}{\xi_p}$	$\frac{\Delta z}{R\xi_p\Psi'}$	$\frac{\Delta z}{R\xi_p\Psi'}$ , $\gamma > \gamma_1$	

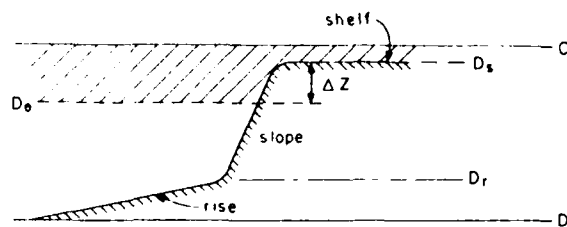


Fig. 9. Schematic section of the continental margin.

with typical values  $\gamma_0 = 37^\circ$  (for  $\Psi = 3\sigma_\Psi = 6.8 \times 10^{-3}$ ) and  $\gamma_1 = 6^\circ$  (for  $R = 1000$  km).

We argue that Table 2 is well represented for CANBARX by the first column only

$$\Gamma \approx \begin{cases} 1 & R\Psi' < \frac{\Delta z}{\xi_p} \\ \frac{\Delta z}{R\xi_p\Psi'} & R\Psi' > \frac{\Delta z}{\xi_p} \end{cases} \quad (13)$$

Since  $2\Delta z/(cT_p) \approx 5.1 \times 10^{-2}$ , values of  $\Psi$  applicable to the first column of Table 2 cover more than 2 standard deviations ( $\sigma_\Psi \approx 2.3 \times 10^{-2}$  for  $\mu_\Psi \approx 3 \times 10^{-2}$  and the presumed half-Gaussian pdf). Also  $\Gamma$  drawn from the second column approaches (13) anyway. That is, for  $R\Psi'$  small (corresponding to  $\gamma \rightarrow 0$ ) and for  $R\Psi'$  large (corresponding to  $\gamma \rightarrow 90^\circ$ ), we see that  $\Gamma$  tends to be (13).

From (13) we can define a crossover range  $R_0$ , based on the mean  $\mu_\Psi$

$$R_0 = \frac{\Delta z}{\xi_p\mu_\Psi} \quad (14)$$

Thus when  $R < R_0$  the acoustic window has high probability of being completely filled by the wedge string, while for  $R > R_0$  it does not, suffering in effect an acoustic loss. We shall use this result in normalization of the reverberation data to obtain interpretable backscatter results.

With  $\mu_\Psi = 3 \times 10^{-2}$  and the foregoing estimate of  $\Delta z$ , the crossover range  $R_0$  is about 190 km. Since  $\Delta z$  and  $\xi_p$  depend upon the measurement system,  $R_0$  is not solely a basin parameter.

#### 4.5 Two-Way Propagation Model

Equation (5) has a simple  $\theta$  integral which, in accordance with section 4.2, we integrate to  $\theta_e$  rather than  $\theta_1$ . We average this result in  $z$  from 0 to  $D_e$ , principally because we do not have a priori knowledge of depth of the relevant scatterers, with the result that the incident field can be expressed as [Smith, 1971].

$$\hat{S}_i = \frac{A}{T_r} \tau_i = \frac{2A}{T_r RD_e} \theta_e e^{-ar} \quad (15)$$

where  $\tau_i$  is the transmission coefficient of the incident field, where  $A/T_r$  can be interpreted as the effective rate of energy propagating in the channel (aside from a factor  $4\pi/\rho c$ ), and where  $T_r$  is the range dependent time spreading of the impulse. The latter is equal to about 1 s per 100 km for the full Arctic acoustic channel ( $\Delta t$  from (7)) but is about 1 s per 500 km for the more energetic components in the depth interval  $0 < z < D_e$ . Data supporting this estimate can be

found in *Kutschale* [1968] and *Milne* [1967]. Simply,  $\bar{S}_i$  is the average spectral density in the effective time interval  $T_r$ .

The component of the intensity vector normal to a scatterer, modelled in macroscale as a wedge, is  $\bar{S}_i \sin \psi'(\rho c)$ . Thus the power flowing normal to the wedge,  $W_i$ , is  $S \bar{S}_i \sin \psi'(\rho c)$  where  $S$  is the wedge surface area occupied by the processing windows. The energy is  $T_r W_i$ , a certain fraction  $b$  of which is reradiated as backscattered energy  $b T_r W_i$ . That is, we take each wedge to have roughness or facets which are the actual backscatter mechanisms, with  $\beta$  defining the mean scattering surface. While such backscattering is known to be highly dependent upon angle between mean scattering surface and wave direction, we represent the process simply by the parameter  $b$ , with justification that the wave/wedge interaction naturally averages over the spread of incident and reflection angles.

The rate of energy backscattered in the time window  $T_p$  is

$$\frac{dE_b}{dt} = \frac{b T_r W_i}{T_p} \quad (16)$$

where time spreading caused by the wedge's range-wise extent is taken to be uniform, justified by the presumed equality in incident energy with depth, and again by the inherent averaging over both incident and reflection angles. We note that the uniform hypothesis requires  $T_p < 2\Delta z/(c\Psi)$ , which holds in our system for  $\Psi < 5 \times 10^{-2}$ , but even when violated still represents the time spreading with acceptable accuracy. We see that wedge time spreading, as measured by  $T_p$ , dominates channel spreading  $T_r$  (and also source duration  $T_s$ ), and justifies (2). That is, scattering and transmission back to the array can be assumed with comfort to be approximated in the time domain as a rectangular function, with smearing due to radiation and transmission occupying an interval reasonably small compared to  $T_p$ .

Conversion of  $dE_b/dt$  to spectral density of the backscattered field  $\bar{S}_b$  is straightforward. Since  $A_b = \rho c E_b/2\pi$  is the equation connecting energy  $E_b$  and strength  $A_b$  of a field radiated over  $2\pi$  steradians, we have in analogy with (15)

$$\bar{S}_b = \frac{A_b S \sin \psi}{2\pi T_p} \tau_i \tau_b = \frac{2AbS \sin \psi}{\pi T_p} \left( \frac{\theta_e \theta_i}{R^2 D_e D_i} \right) e^{-2\alpha R} \quad (17)$$

Note that  $\bar{S}_b$  does not depend upon  $T_r$ , since the incident spectral density and backscatter energy rate depend inversely and directly upon  $T_r$ , respectively. It is simple to show that the scattering area is given by

$$S = \frac{\Gamma R \xi_p c T_p}{2 \cos \psi \cos \psi'} \quad (18)$$

which takes on various values from  $\Gamma$  in Table 2 or as approximated for CANBARX in (13).

With reference to (1) the reverberation signal  $r$  is modeled as  $T_p \bar{S}_b/A$ , with dimensions of inverse-square length, and from (17) and (18) is

$$r = \left( \frac{b\Psi}{\cos \psi'} \right) \left( \frac{R \xi_p c T_p/2}{2\pi} \right) \tau_i \tau_b \left\{ \frac{1}{R \xi_p \Psi'} \right\} \quad (19)$$

where the split values refer to conditions in the same order as in (13). We see that for small  $R$  the reverberation signal varies as  $R^{-1}$ , while for large  $R$  it goes as  $R^{-2}$ . Also at large

$R$  the signal does not depend upon  $\xi_p$ , the resolution being  $\Delta z/(R\Psi')$ , but the resolution displayed will depend upon the steering steps used.

Equation (19) is seen to justify (2), for it gives a linear dependence of  $r$  upon  $T_p$ . Implicitly,  $T_p$  must be no more than  $2\Delta z/(c\Psi)$ , and we take 20 s as the largest practical value for our experiments.

Let us write  $\bar{r}$  as the estimate of  $r$  from measurements in the time window  $T_p$ . Then the model provided by (19) can be restated as

$$\eta = \frac{b\bar{\Psi}}{\cos \psi'} = \bar{r} \frac{4\pi}{R \xi_p c T_p} (\tau_i \tau_b)^{-1} \left\{ \frac{1}{R_0 \mu_\Psi} \right\} \quad (20)$$

in which we have used (14) for  $R_0$  and where  $\eta$  is interpreted as an estimate from measurements of a backscattering quantity. We know all parameters on the rhs except for  $\Psi'$  of which we do not have a priori knowledge. Thus we average over the angle parameters of the basin, with the result

$$\mu_\eta = \left\langle \frac{b\bar{\Psi}}{\cos \psi'} \right\rangle = \bar{r} \frac{4\pi}{R \xi_p c T_p} (\tau_i \tau_b)^{-1} \begin{cases} 1 & R < R_0 \\ R/R_0 & R > R_0 \end{cases} \quad (21)$$

where  $\mu_\eta$  is the angle average of the lhs of (20). As a model of backscattering, (21) normalizes the measurements to yield physically comparable results throughout the basin. Systematic changes in  $\mu_\eta$  from some overall norm can then be ascribed to local 'abnormalities' in  $b$  or  $\Psi$ , although we have not as yet separated these in our results.

#### 4.6 Attenuation Coefficient

Parameters in (21) have been estimated in prior sections, except for  $\exp[-2\alpha R]$  appearing in  $\tau_i \tau_b$ ; we arrive at this estimate here. As is customary, we write  $\alpha = 4.34a$  so that the loss coefficient is expressed in dB per unit distance. At low frequencies, loss mechanism candidates are (1) boric acid/borate relaxation [Fisher and Simmons, 1977], (2) underice scattering [Diachok, 1976], and (3) volume scattering [Mellen et al., 1974].

At 9 Hz the first is estimated to be  $\alpha_1 \approx 6 \times 10^{-6}$  dB/km, with frequency dependence of  $f^2$ . Thus the first mechanism has negligible effect in two-way transmission out to a range of 2500 km. Uncertainties associated with  $\alpha_1$  pertain to the pH of Arctic waters, but are within a factor of 2 using other oceans as a guide [Lovett, 1980].

The second mechanism may well be dominant in CANBARX, or at least nonnegligible. Diachok modeled ice scattering as reflections from cylindrical keels. With use of his model and parameter estimates (10.5 keels/km, keel depth 4.8 m, and keel half-width 9.8 m), we find  $\alpha_2 \approx 3 \times 10^{-4}$  dB/km at 9 Hz. On the other hand, Bass and Fuks [1979] modeled loss in a nonrefracting parallel-plate waveguide with Gaussian roughness of rms depth  $\zeta_i$  and correlation radius  $\Lambda_i$  on one surface. With use of their formula adjusted to account for refraction, and with estimates  $\zeta_i \approx 2.4$  m and  $\Lambda_i \approx 70$  m [Wadhams and Horne, 1980; Lowry and Wadhams, 1979; Rothrock and Thorndike, 1980], we get  $\alpha_2 \approx 2 \times 10^{-3}$  dB/km. The former estimate would have a 3 dB effect at 2500 km, the latter 10 dB, and correspondingly less at smaller  $R$ . The frequency dependence of  $\alpha_2$  is  $f^3$  (Diachok)



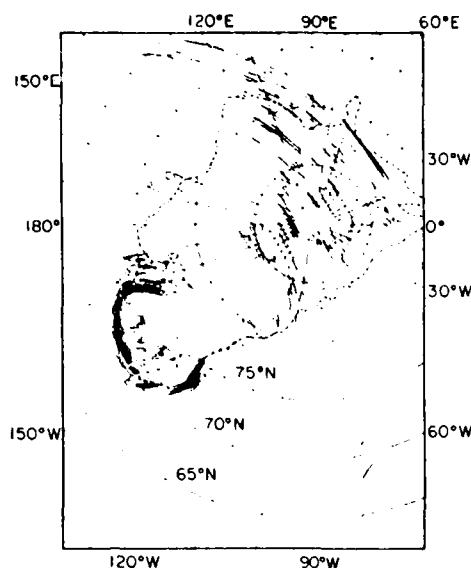


Fig. 10. Backscattering levels for the Arctic basin (experiment 14). Contours:  $-32$ ,  $-36$ ,  $-40$  dB, with levels in excess of  $-32$  dB filled in for emphasis. The 500 m depth contour from a standard chart is shown for orientation.  $\alpha = 0.001$  dB/km.

or  $f^4$  (Bass and Fuks). A review by Buck [1981] of sound transmission data in the Arctic gives comparable results at 9 Hz ( $\alpha_2 = 3 \times 10^{-3}$  dB/km for  $\zeta_i = 2$  m), but he finds the data to have a frequency dependence of  $f$ .

Another possibly dominant loss mechanism at 9 Hz is the third one, volume scattering. A recent review [Kibblewhite and Hampton, 1980] has shown a mean value  $\alpha_3 = 10^{-3}$  dB/km with standard deviation of the same order for seven experiments in various regions of the deep Atlantic and Pacific. (Data in the eastern North Pacific for acoustic paths through the subarctic convergence were excluded by the review authors as being anomalously high.) Models exist which connect volume scattering loss with sound speed

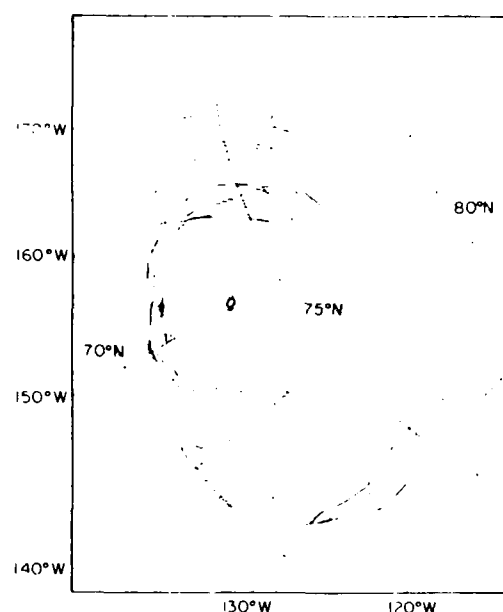


Fig. 12. Close-in backscattering levels, experiment 14. Contours:  $-27$  to  $-36$  dB in 3 dB steps.  $\alpha = 0.001$  dB/km.

fluctuations [Mellen *et al.*, 1974] which, in turn, can be caused by internal waves [Mellen *et al.*, 1976; Flatte, 1979], among many possible mechanisms. The mean estimate of  $\alpha_3$  would have a 5 dB effect at 2500 km, with negligible effect and a 10 dB effect at the 1 standard deviation extremes.  $\alpha_3$  is frequency independent.

In the absence during CANBARX of direct ice scattering data, and data on internal waves and other water column fluctuations which could help fix  $\alpha$ , we adopt as a nominal value,  $\alpha = 10^{-3}$  dB/km. This value has the virtue of being near the center of uncertainty, from which we might infer 'better' values upon inspection of the backscattering levels.

## 5. BACKSCATTERING DATA

With the nominal value  $\alpha = 10^{-3}$  dB/km, and other parameters estimated previously, we can chart the backscatter level

$$BL = 10 \log \mu_{\eta}, \text{ dB} \quad (22)$$

where  $\mu_{\eta}$ , with use of (21), can be found from the measured reverberation level. Each of the backscatter charts we will show has been cleansed of array side lobes, since maximum likelihood processing can introduce spurious values at angles other than those corresponding to real returns. In essence we have sharply attenuated these side lobes via an algorithm related to the directivity of strong returns [Williams, 1981].

Figure 10 shows backscatter from the Arctic basin, with strong returns from some of the more distant regions. At the scale shown, the chart is difficult to interpret in detail, but it is clear that CANBARX provides wide area information on backscattering.

Contours from different shots agree within about 1 dB, as Figure 11 shows. This figure, for the Beaufort Sea, also displays more energetic levels, with each contour level 4 dB higher than in Figure 10. Further details in the Beaufort Sea can be seen in Figure 12, which has the same lowest contour as in Figure 11, but steps up in finer increments. Between about 156°W and 163°W the Northwind Escarpment shows

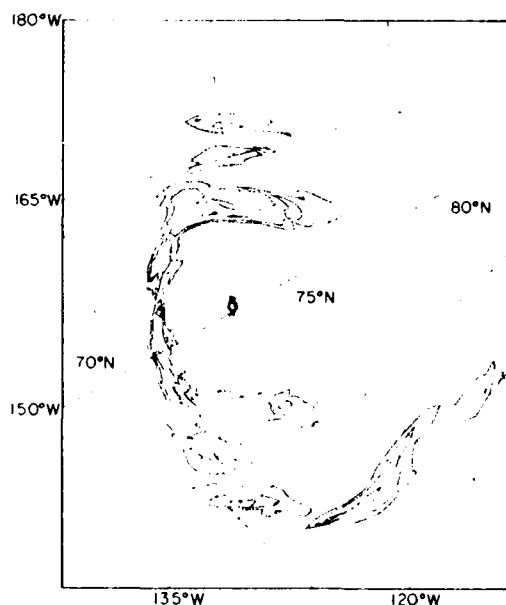


Fig. 11. Close-in backscattering levels for two different shots, both 200 kg. Dotted line experiment 13, solid line experiment 14. Contours:  $-28$ ,  $-32$ ,  $-36$  dB.  $\alpha = 0.001$  dB/km.

boldly, with Chukchi features showing beyond. To the south the Alaska slope also shows boldly and continues toward the Canadian Archipelago, with the slopes off Tuktoyaktuk, Banks Island, and Prince Patrick Island also showing well (see 71°N, 135°W; 73°N, 128°W; and 77°N, 125°W, respectively). These Beaufort Sea data are little affected by the aforementioned uncertainties in  $\alpha$ , since  $\alpha R$  is reasonably small for the range of  $R$  encountered.

A prominent backscattering feature often omitted in existing topographic charts, is centered at about 73.2°N, 139.0°W. While some charts indicate one or more features in this area [e.g., *De Leeuw*, 1967; *National Geographic*, 1971; *Stefansson*, 1921; *U.S. Army et al.*, 1971] none shows them of scale or relief sufficient to explain the observed backscatter. For example, we would expect the feature to be shallower than 1000 m and/or to have steep slopes as in the Northwind Escarpment. Standard bathymetric measurements in the area would provide the ultimate test of its reality, but in the interim we are encouraged to accept it not only on the basis of the present result, but also because magnetic anomaly data are supportive [*Taylor et al.*, 1981]. We tentatively name this the 'G. Leonard Johnson Feature' to honor the individual who most encouraged our work.

In some ways, data beyond about 1500 km are disappointing or unclear in physical message. Figure 10 shows some returns on 'land'; these must be due to secondary basin backscattering paths which we have not as yet unraveled. Inability to follow the shape of the continental slope at long ranges, also to be seen in Figure 10, is a consequence of finite azimuthal resolution which is as gross as 250 km or so at large  $R$ .

One may also question the transmission/backscattering models and/or estimates used by us, at least because the most distant levels seem only occasionally to be as high as those close in. We offer some discussion points on this:

1. A larger value of  $\alpha$  would have 'brightened' the distant returns. Enhancement by 5 dB or more at 2500 km would seem appropriate, but in view of point 4 we are reluctant to ascribe all of it to a too low value of  $\alpha$ .

2. Our model holds that the incident energy below about 1000 m can be neglected. We see, however, that the Northwind Escarpment, believed to be no shallower than about 1000 m, comes in strongly. We interpret this as evidence of abnormally large slopes in this feature, and therefore our model should be extended to allow the combination of weakly energized but strong scatterers at depth.

3. The attitude maintained in point 2 on concentration of energy above about 1000 m, also helps explain the returns from features beyond the Northwind Escarpment (see vicinity of 78°N, 160°W in Figure 10). That we have irradiated them sufficiently to obtain returns is clear; but not included in the present transmission model is loss caused by the shielding feature in the return direction. A rough estimate of the return loss is 3–6 dB over the Chukchi Plateau, and such losses applied to the normalized data would enhance the entire Siberian slope, as well as particular features along it.

4. Similar arguments help explain in part the relatively weak but measurable returns from the European Slope and from Greenland and the Canadian Archipelago beyond the Alpha Ridge. The Alpha, Lomonosov, and mid-Arctic ridges probably cause return losses of a few dB each, and also may time-spread the signals in such a way as to blur the return patterns.

## 6. SPECULATIONS ON BASIN ROUGHNESS

In an attempt to understand the backscattering mechanism underlying the observed results, we ascribe to the slope the following characteristics: (1) It is a rough surface, statistically homogeneous throughout the Arctic. (2) the roughness height measured from the mean surface has a Gaussian pdf with  $\xi^2$  its mean square value, and (3) the heights have an auto-correlation function  $\exp\{-y^2/\Lambda^2\}$  with  $y$  the in-plane distance separating two observation positions (isotropy on each wedge surface). We adopt standard scattering theory [*Beckmann and Spizzichino*, 1963] which, in small angle approximation, yields the energy scattering coefficient in the backscattering plane

$$b_s = \frac{1}{8} k^4 \xi^2 \Lambda^2 (\Phi_i + \Phi_h)^4 \exp\left[-\frac{k^2 \Lambda^2}{16} (\Phi_i^2 - \Phi_h^2)^2\right] \quad (23)$$

This equation is valid for  $k^2 \Lambda^2 \gg 1$  and  $k^2 \xi^2 (\Phi_i + \Phi_h)^2 \ll 1$ , where  $k$  is the wave number, and  $\Phi = \phi + \psi$  is the ray angle measured from the wedge for each of the incident and backscatter fields. The first wave number condition restricts attention to features whose jaggedness is not abrupt on a scale less than a quarter wavelength, and the second classifies the surface as only slightly rough, as all surfaces must be near grazing incidence. We believe these conditions are physically sensible, at least in the main.

Equation (23) can be simplified further. The argument of the exponential will be small if  $k\Lambda < 4/\Phi^2$ . From equation (10) the maximum value of  $\Phi^2$  is  $4\psi\theta$ . Thus if  $k\Lambda < (\psi\theta)^{-1}$  we have

$$b_s = \frac{1}{8} k^4 \xi^2 \Lambda^2 (\Phi_i + \Phi_h)^4 \quad (24)$$

We see that  $1 < k\Lambda < 10^2$  would satisfy both the latter and earlier conditions on  $k\Lambda$ . The angle average of  $b_s$  is then easy to calculate and is

$$b = 2k^4 \xi^2 \Lambda^2 \theta_i \theta_e \psi^2 \left[ \frac{2}{3} + \frac{1}{5} \left( \frac{\theta_i}{\theta_e} + \frac{\theta_e}{\theta_i} \right) + \frac{1}{2} \left\{ \left( \frac{\theta_i}{\theta_e} \right)^{1/2} + \left( \frac{\theta_e}{\theta_i} \right)^{1/2} \right\}^2 \right] \quad (25)$$

where the interval averaged over is  $(4\psi\theta_e)^{1/2}$  and  $(4\psi\theta_i)^{1/2}$  for  $\Phi_i$  and  $\Phi_h$ , respectively.

Numerically we have, with  $\theta_e = 0.14$  and  $\theta_i = 0.30$ ,  $b = (0.18)k^4 \xi^2 \Lambda^2 \psi^2$  which we used in the lhs of equation (21). Thus  $\mu_\eta \approx (0.18)k^4 \xi^2 \Lambda^2 \langle \psi^2 \rangle$ . With the use of the half-Gaussian pdf for  $\Psi$  we get  $\langle \psi^2 \rangle = \pi \mu_\Psi^{-1}$ , and with the estimate  $\mu_\Psi = 3 \times 10^{-2}$  and the datum  $\mu_\eta \approx 6 \times 10^{-4}$  (i.e.,  $BL \sim -32$  dB as a slope average), we estimate

$$k^2 \xi \Lambda \sim 6.3, \quad (26)$$

or  $\xi \Lambda \sim 4500 \text{ m}^2$ . It is relevant to add that use of  $\eta$  directly from equation (20) without basin averaging leads to the same estimate of  $k^2 \xi \Lambda$  (e.g.,  $\eta \sim 10^{-3}$ ,  $\psi \sim 4 \times 10^{-2}$ , and  $\psi' \sim 2 \times 10^{-2}$ , the latter two at factors of about 1 standard deviation away from the mean).

We can't extract more than the estimate of  $4500 \text{ m}^2$  for the product of rms height and correlation radius. We note,

however, that the rms roughness slope, for small slopes, is  $2^{1/2}\zeta/\lambda$ , and in the range of the model's validity ( $1 < \zeta < 10^2$  m and  $3 \times 10^3 > \lambda > 30$  m) the rms slope is between  $3 \times 10^{-4}$  and some number  $O(1)$ , comfortably bracketing the roughness slope one might expect.

There is another possible insight on basin backscattering. It might have been expected that the rough underside of the ice would be at least as important in backscattering as the continental margin. But our data are dominated by the margin, at least out to  $R \sim 2000$  km. If we take the observed levels in the center of the east Arctic Ocean as an upper limit of underice backscattering ( $\sim 40$  dB, see Figure 10) we find with suitable adjustments that the ice product  $\zeta\lambda$ , is no more than  $350$  m<sup>2</sup>. (8 dB less than mean slope levels, 10 dB less because the acoustic window always fully intersects the ice, 11 dB less because ray angles striking the ice are on average about 1.9 larger, 4 dB more because  $\alpha$  is probably twice the nominal value, 3 dB more because loss in round trip propagation to the East Arctic did not account for the Alpha, Lomonosov, and mid-Arctic Ridges.) We previously estimated these parameters in our discussion of transmission, and their product ( $170$  m<sup>2</sup>) is about 1/2 of that deduced here as an upper limit. Thus, some support is evident for the importance of ice scattering, and for a value of  $\alpha$  larger than the nominal one used, perhaps as large as  $\alpha = 2 \times 10^{-3}$  dB/km. Also a possible explanation for the diffuseness of the distant returns, additional to those offered in section 5, may be underice backscattering. Discrimination against such signals depends upon  $\xi_p$ , and thus higher resolution systems could improve distant returns, to the extent they are limited by ice scattering.

We do not wish to overstate the firmness of equation (26) nor the analogous conclusions on ice backscattering. Based on absolute error equation (26) is accurate to no better than a factor of 2 (3 dB), and must be considered significantly worse given the guesses we have had to make on  $\psi$  and its pdf. The 'adjustments' used to reach conclusions on ice backscattering, though perhaps reasonable, are pure speculations and need more comprehensive research to gain credence.

Finally, a note on experiment design is appropriate. The expected backscatter is proportional to  $f^4$ , so it might be argued that higher frequency measurements are better, especially given that array performance would improve. But losses also would increase and unfortunately might be as drastic as  $\exp[-nf^4]$ , where  $n$  is some range dependent number. Also the source spectral density goes as  $f^{-2}$ , and the noise as  $f^0$  to  $f^{-2}$ , so it might turn out that higher frequencies are not better after all.

## 7. CONCLUSIONS

Compared with omnidirectional systems, an array can significantly enrich the quality of reverberation or backscatter data. CANBARX data provide new insights on basin features related to backscattering, including possible delineation of new or little explored topographic features, and estimation of roughness parameters for the continental slope. We are on the whole pleased with the promise of this technique and, in its first use in CANBARX, have gained experience essential to further development.

Many improvements and extensions of the results presented here can be suggested: (1) Clearly, further analysis of the tentative G. Leonard Johnson Feature, and other 'abnormal' returns, should be carried out. (2) Backscattering charts for

center frequencies other than 9 Hz should be prepared to check the frequency dependence of the many physical processes involved. (3) More careful modeling of the ice backscatter process would be useful not only in clarifying its relationship to margin backscattering, but also for its intrinsic value. There is promise that ice backscattering in the manner treated here can be used to gain synoptic information on ice roughness over large areas. (4) Statistical analysis of the temporal extent of the signal envelopes can yield the pdf of  $\psi$ , which can be used to check or modify the one assumed, and thus should be done. (5) Other measurement locations should be tried to test the generality of the method, and one such has been undertaken [Baggeroer and Dyer, 1980]. (6) A series of shots at various depths would illuminate other features in the basin, and should be carried out.

**Acknowledgments.** We thank our colleagues in the CANBARX team whose efforts made our work possible. Particular acknowledgment is extended to Keith von der Heydt, Thomas O'Brien, and Kenneth Prada of the Woods Hole Oceanographic Institution for successful planning, implementation, and deployment of the data acquisition and recording system; to George Shepard for assistance in data acquisition; and to Henry Kutschale of Lamont-Doherty Geological Observatory with whom our ideas on basin backscattering were first shared and who provided wise advice on both scientific questions and experimental matters. The Arctic Office of ONR provided funds under the overall management of Ronald McGregor and the able scientific support of Leonard Johnson. Additional support was provided by the Ocean Science Office of ONR, and by M.I.T.

## REFERENCES

- Baggeroer, A. B., *Applications of Digital Signal Processing*, edited by A. V. Oppenheim, chap. 6, Prentice-Hall, Englewood Cliffs, N.J., 1978.
- Baggeroer, A. B., and I. Dyer, FRAM II in Eastern Arctic Ocean, *Eos Trans. AGU*, 61, 217, 221, 222, 1980.
- Baggeroer, A. B., and R. Falconer, Array refraction profiles and crustal models of the Canada Basin, *J. Geophys. Res.*, 87, 5461-5476, 1982.
- Bass, F. G., and I. M. Fuks, *Wave Scattering from Statistically Rough Surfaces*, Pergamon, p. 468, New York, 1979.
- Beckmann, P., and A. Spizzichino, *The Scattering of Electromagnetic Waves from Rough Surfaces*, p. 86, Pergamon, New York, 1963.
- Blatstein, I. M., Ocean basin reverberation at very low frequencies (Abstract), *J. Acoust. Soc. Am.*, 64, 564, 1978.
- Buck, B. M., Preliminary underice propagation models based on synoptic ice roughness, TR-30, Polar Res. Lab., Santa Barbara, Calif., 1981.
- Canadian Hydrographic Service, General Bathymetric Chart of the Oceans, Map No. 5-17, Ottawa, 1979.
- Capon, J., *Nonlinear Methods of Spectral Analysis*, edited by S. Haykin, Chap. 6, Springer-Verlag, Berlin, 1979.
- De Leeuw, M. M., New Canadian bathymetric chart of the western Arctic Ocean north of 72°, *Deep Sea Res.*, 14, 489-504, 1967.
- diNapoli, F. R., D. Viccione, and H. Kutschale, The Arctic Channel: An acoustic waveguide, TM 781078, Naval Underwater Systems Center, New London, Conn., 1978.
- Diachok, O. I., Effects of sea ice ridges on sound propagation in the Arctic Ocean, *J. Acoust. Soc. Am.*, 59, 1110-1120, 1976.
- Fisher, F. H., and V. P. Simmons, Sound absorption in sea water, *J. Acoust. Soc. Am.*, 62, 558-564, 1977.
- Flatte, S. M. (ed.), *Sound Transmission Through a Fluctuating Ocean*, p. 234, Cambridge University Press, New York, 1979.
- Gaspin, J. B., J. A. Goertner, and I. M. Blatstein, Determination of acoustic source levels for shallow underwater explosions, *J. Acoust. Soc. Am.*, 66, 1453-1462, 1979.
- Goertner, J. A., and I. M. Blatstein, Computer model for predicting acoustic reverberation from underwater explosions, *IEEE E. Oceans '75*, 227-232, 1975.
- Kutschale, H., Arctic hydroacoustics, *Arctic*, 22, 246-264, 1969.
- Kutschale, H., Long-range sound propagation in the Arctic Ocean,

- in *Arctic Drifting Stations*, edited by J. E. Sater, pp. 281-295, Arctic Institute of North America, Calgary, Alberta, Canada, 1968.
- Lovett, J. R., Geographic variation of low frequency sound absorption in the Atlantic, Indian, and Pacific oceans, *J. Acoust. Soc. Am.*, **67**, 338-340, 1980.
- Lowry, R. T., and P. Wadhams, On the statistical distribution of pressure ridges in sea ice, *J. Geophys. Res.*, **84**, 2487-2494, 1979.
- Malme, C. I., J. Carbonell, and I. Dyer, Mechanisms in the generation of air-blasts by underwater explosions, *Rep. 66-68*, Naval Ordnance Lab., White Oak, Md., 1966.
- McDonough, R. N., *Nonlinear Methods of Spectral Analysis*, edited by S. Haykin, chap. 6, Springer-Verlag, Berlin, 1979.
- Mellen, R. H., D. G. Browning, and J. M. Ross, Attenuation in randomly inhomogeneous sound channels, *J. Acoust. Soc. Am.*, **56**, 80-82, 1974.
- Mellen, R. H., and H. W. Marsh, Underwater sound reverberation in the Arctic Ocean, *J. Acoust. Soc. Am.*, **35**, 1645-1648, 1963.
- Milne, A. R., Sound propagation and ambient noise under sea ice, in *Underwater Acoustics*, vol. 2, edited by V. M. Albers, chap. 7, Plenum, New York, 1967.
- National Geographic Society, *Arctic Ocean Floor*, Washington, D. C., 1971.
- Rothrock, D. A., and A. S. Thorndike, Geometric properties of the underside of sea ice, *J. Geophys. Res.*, **85**, 3955-3963, 1980.
- Smith, P. W. Jr., Averaged impulse response of a shallow-water channel, *J. Acoust. Soc. Am.*, **50**, 332-336, 1971.
- Smith, P. W. Jr., Averaged sound transmission in range-dependent channels, *J. Acoust. Soc. Am.*, **55**, 1197-1204, 1974.
- Smith, P. W. Jr., Spatial coherence in multipath or multimodal channels, *J. Acoust. Soc. Am.*, **60**, 305-310, 1976.
- Stefansson, V., *The Friendly Arctic*, MacMillan, New York, 1921.
- Taylor, P. T., P. R. Vogt, G. L. Jackson, and L. C. Kovacs, Origin of the Canada Basin: Considerations of Magnetic Data, paper presented at 21st General Assembly IASPEI, London, Canada, 1981.
- Urick, R. J., *Principles of Underwater Sound*, 2nd Ed., McGraw Hill, New York, 1975.
- U.S. Army Topographic Command and U.S. Navy Oceanographic Office, *The World, Ser. 1142*, Washington, D. C., 1971.
- Wadhams, P., and R. J. Horne, An analysis of ice profiles obtained by submarine sonar in the Beaufort Sea, *J. Glaciol.*, **25**, 401-424, 1980.
- Weston, D. E., Acoustic flux formulas for range-dependent ocean ducts, *J. Acoust. Soc. Am.*, **68**, 261-281, 1980.
- Weston, D. E., Underwater explosions as acoustic sources, *Proc. Phys. Soc.*, **76**, 233-249, 1960.
- Williams, R. J., Backscattering of low frequency sound from the topographic features of the arctic ocean basin, Thesis, Mass. Inst. of Tech., Cambridge, Mass., 1981.
- Zittel, J. D., Ocean basin reverberation, Thesis, Mass. Inst. of Tech. and the Woods Hole Oceanogr. Inst., 1979.

(Received April 2, 1982;  
revised July 30, 1982;  
accepted August 9, 1982.)